

GSI-Preprint-2000-49, November 2000

## Shadowing Effects on Vector Boson Production

R. Vogt

*GSI, Planckstrasse 1, D-64291 Darmstadt*

*Nuclear Science Division, Lawrence Berkeley National Laboratory, Berkeley, CA 94720, USA*

*Physics Department, University of California, Davis, CA 95616, USA*

### Abstract

We explore how nuclear modifications to the nucleon structure functions, shadowing, affect massive gauge boson production in heavy ion collisions at different impact parameters. We assume that the nuclear modifications are proportional to the local nuclear density. We calculate the dependence of  $Z^0$ ,  $W^+$  and  $W^-$  production on rapidity and impact parameter in Pb+Pb collisions at 5.5 TeV/nucleon to study quark shadowing at high  $Q^2$ . We also compare our Pb+Pb results to the  $pp$  rapidity distributions at 14 TeV.

The heavy ion collisions at the LHC will be a rich testing ground for hard processes which should dominate particle production [1,2]. One of the most promising signatures of quark-gluon plasma production at the CERN SPS is  $J/\psi$  suppression [3,4] which has been compared to the Drell-Yan continuum in the mass range  $2.9 < m < 4.5$  GeV. Both the production of  $J/\psi$  and Drell-Yan pairs are calculable in perturbative QCD. At the LHC, quarkonium suppression will be difficult to compare to the dilepton continuum due to contributions from  $c\bar{c}$  and  $b\bar{b}$  decays which have large uncertainties in nuclear collisions [5]. Since the low mass dilepton continuum is expected to be dominated by  $b\bar{b}$  decays, the  $Z^0$  was suggested as an alternative reference process for quarkonium suppression at the LHC [6,7]. There are two difficulties with using the  $Z^0$  as a baseline for quarkonium suppression: the large mass differences,  $m_{Z^0} \gg m_Y, m_{J/\psi}$ , and the difference in production mechanisms, predominantly  $q\bar{q}$  for the  $Z^0$  and  $gg$  for quarkonium. Both these differences are important as far as nuclear effects are concerned. However, the differences that reduce the value of the  $Z^0$  as a baseline process are the same that make it an interesting object of study itself—the  $Z^0$  provides a unique opportunity to study quark shadowing at high  $Q^2$ . Therefore, in this paper we examine the possible effects of shadowing on  $Z^0$  production as well as  $W^+$  and  $W^-$  production which are also quark dominated. The impact parameter dependence of the shadowing effect will also be shown.

We further address the issue of how to determine the shadowing effect. Since isospin will play an important role in quark-dominated processes, the comparison between Pb+Pb interactions with and without shadowing is less useful than in gluon-dominated processes such as heavy quark production [8]. In addition, the first, best,  $pp$  data will be at the maximum LHC energy of 14 TeV. Therefore we will also present the predicted rapidity distributions in Pb+Pb collisions at 5.5 TeV/nucleon and the  $pp$  distributions at 14 TeV as well as the Pb+Pb/ $pp$  ratios at the two energies.

The electroweak production and decay channels of the massive vector bosons make them excellent candidates for shadowing studies since no hadronic final-state rescattering is possible. The  $Z^0$  itself, with a 3.37% branching ratio to lepton pairs, will be easily observable by reconstructing the peak. Full reconstruction of the leptonic  $W^\pm$  decays,  $W^\pm \rightarrow l^\pm \nu$ , is not possible due to the missing energy given to the undetected neutrino but charged leptons with momenta greater than 40 GeV should be prominent. This technique has been used at the Tevatron to measure the asymmetry between  $W^+$  and  $W^-$  production through their lepton decays since this asymmetry is sensitive to the ratio  $f_d^p/f_u^p$  at intermediate values of  $x$  and high  $Q^2$  [9]. If the charged leptons from  $W^\pm$  decays can be identified in heavy ion collisions, such asymmetry measurements may also be employed at the LHC to reduce systematics and obtain a more meaningful determination of the  $Q^2$  dependence of quark shadowing in the nucleus.

The leading order, LO, cross section per nucleon for nuclei  $A$  and  $B$  colliding at impact parameter  $b$  and producing a vector boson  $V$  with mass  $m$  at scale  $Q$  is

$$\frac{1}{AB} \frac{d\sigma_{AB}^V}{dy d^2b d^2r} = \sum_{i,j} \int dz dz' F_i^A(x_1, Q^2, \vec{r}, z) F_j^B(x_2, Q^2, \vec{b} - \vec{r}, z') \frac{d\hat{\sigma}_{ij}^V}{dy}, \quad (1)$$

where  $\hat{\sigma}_{ij}^V$  is the partonic  $ij \rightarrow V$  cross section. We assume that the parton densities  $F_i^A(x, Q^2, \vec{r}, z)$  can be factorized into  $x$  and  $Q^2$  independent nuclear density distributions, position and nuclear-number independent nucleon parton densities, and a shadowing func-

tion  $S^i(A, x, Q^2, \vec{r}, z)$  that describes the modification of the nuclear structure functions in position and momentum space. Thus we have

$$\begin{aligned} F_i^A(x, Q^2, \vec{r}, z) &= \rho_A(s) S^i(A, x, Q^2, \vec{r}, z) f_i^N(x, Q^2) \\ F_j^B(x, Q^2, \vec{b} - \vec{r}, z') &= \rho_B(s') S^j(B, x, Q^2, \vec{b} - \vec{r}, z') f_j^N(x, Q^2) \end{aligned} \quad (2)$$

where  $f_i^N(x, Q^2)$  are the densities of parton  $i$  in the nucleon and the radial variables  $s$  and  $s'$  are  $s = \sqrt{r^2 + z^2}$  and  $s' = \sqrt{|\vec{b} - \vec{r}|^2 + z'^2}$ . In the absence of nuclear modifications,  $S^i(A, x, Q^2, \vec{r}, z) \equiv 1$ . The nuclear density distribution is a Woods-Saxon,

$$\rho_A(s) = \rho_0 \frac{1 + \omega(s/R_A)^2}{1 + \exp[(s - R_A)/d]} . \quad (3)$$

Electron scattering data [10] are used to fix the parameters  $R_A$ ,  $d$ ,  $\omega$  and  $\rho_0$ .

Experiments [11] have shown that the proton and neutron structure functions are modified in the nucleus. For momentum fractions  $x < 0.1$  and  $0.3 < x < 0.7$ , a depletion is observed in a large nucleus relative to a light nucleus such as the deuteron. The low  $x$ , shadowing, region and the larger  $x$ , EMC, region is bridged by an enhancement at  $0.1 < x < 0.3$  called antishadowing. Many theoretical explanations of this effect have been proposed. For example, if the modification is due to gluon recombination [12], then the degree of modification should depend directly on the local gluon density and hence on the spatial position of the interaction within the nucleus. Nuclear binding and rescaling models also predict that the structure function depends on the local density [13]. Since no model can describe the effect over all  $x$ , we rely on parameterizations of the nuclear modifications.

Most typical structure function measurements are insensitive to any spatial dependence and thus average over the entire nucleus. One experiment using a bubble chamber found that the structure function does vary spatially but could not determine the dependence on impact parameter [14]. In a nuclear collision, the impact parameter can be determined from the transverse energy production. The spatial dependence of shadowing on transverse energy production has already been considered [2,15]. The effects of spatially inhomogeneous shadowing on heavy quark [8,16], quarkonium, and Drell-Yan [2,17] production in heavy ion collisions has also been discussed previously.

At LO, the partonic cross sections for the  $2 \rightarrow 1$  production of vector bosons are quite simple [18]

$$\hat{\sigma}_{ij}^{Z^0} = 8\pi \frac{G_F}{\sqrt{2}} [(g_V^i)^2 + (g_A^i)^2] m_Z^2 \delta(\hat{s} - m_Z^2) \quad (4)$$

$$\hat{\sigma}_{ij}^{W^\pm} = 2\pi \frac{G_F}{\sqrt{2}} |V_{ij}|^2 m_W^2 \delta(\hat{s} - m_W^2) \quad (5)$$

where  $G_F = 1.16639 \times 10^{-5}$  GeV $^2$ ,  $m_Z = 91.187$  GeV, and  $m_W = 80.41$  GeV. For a given flavor  $i$ , the sum of the squared vector and axial vector couplings are  $(g_V^i)^2 + (g_A^i)^2 = (1/8)(1 - 4|e_i|x_W + 8e_i^2x_W^2)$  where  $x_W = \sin^2 \theta_W = 1 - m_W^2/m_Z^2$ . For the  $W^+$  and  $W^-$ , we assume only the matrix elements  $|V_{ud}|$  and  $|V_{us}|$  are important. These two matrix elements are defined through the Cabibbo angle  $\theta_C$  as  $V_{ud} = \cos \theta_C$  and  $V_{us} = \sin \theta_C$  with  $\sin \theta_C \approx 0.22$ . The vector boson rapidity distribution is obtained by adding the delta function  $\delta(y -$

$(1/2) \ln(x_1/x_2))$  and convoluting over the parton densities with  $\hat{s} = sx_1x_2$ . These two ingredients fix  $x_1$  and  $x_2$  so that  $x_{1,2} = (m_V/\sqrt{s}) \exp(\pm y)$ .

In  $AB$  collisions, the cross section per nucleon must include the nuclear isospin since, in general,  $\sigma_{pp}^V \neq \sigma_{pn}^V \neq \sigma_{np}^V \neq \sigma_{nn}^V$ . Then the integrand of Eq. (1), including only the shadowing functions and the partonic cross section, is

$$\begin{aligned} S^i(A, x_1) S^j(B, x_2) f_i^N(x_1, Q^2) f_j^N(x_2, Q^2) \frac{d\hat{\sigma}_{ij}^{Z^0}}{dy} = & K \frac{\pi}{3} \frac{G_F}{\sqrt{2}} \frac{x_1 x_2}{AB} \{ \\ & \times [1 - \frac{8}{3}x_W + \frac{32}{9}x_W^2] (S^u(A, x_1) S^{\bar{u}}(B, x_2) \{ Z_A f_u^p(x_1, Q^2) + N_A f_u^n(x_1, Q^2) \} \\ & \times \{ Z_B f_{\bar{u}}^p(x_2, Q^2) + N_B f_{\bar{u}}^n(x_2, Q^2) \} + [u \leftrightarrow \bar{u}]) \\ & + [1 - \frac{4}{3}x_W + \frac{8}{9}x_W^2] (S^d(A, x_1) S^{\bar{d}}(B, x_2) \{ Z_A f_d^p(x_1, Q^2) + N_A f_d^n(x_1, Q^2) \} \\ & \times \{ Z_B f_{\bar{d}}^p(x_2, Q^2) + N_B f_{\bar{d}}^n(x_2, Q^2) \} + [d \leftrightarrow \bar{d}]) \\ & + 2AB S^s(A, x_1) S^{\bar{s}}(B, x_2) f_s^p(x_1, Q^2) f_{\bar{s}}^n(x_2, Q^2) \} \} \end{aligned} \quad (6)$$

$$\begin{aligned} S^i(A, x_1) S^j(B, x_2) f_i^N(x_1, Q^2) f_j^N(x_2, Q^2) \frac{d\hat{\sigma}_{ij}^{W^+}}{dy} = & K \frac{2\pi}{3} \frac{G_F}{\sqrt{2}} \frac{x_1 x_2}{AB} \{ \\ & \times \cos^2 \theta_C (S^u(A, x_1) S^{\bar{d}}(B, x_2) \{ Z_A f_u^p(x_1, Q^2) + N_A f_u^n(x_1, Q^2) \} \\ & \times \{ Z_B f_{\bar{d}}^p(x_2, Q^2) + N_B f_{\bar{d}}^n(x_2, Q^2) \} + [u \leftrightarrow \bar{d}]) \\ & + \sin^2 \theta_C (S^u(A, x_1) S^{\bar{s}}(B, x_2) \{ Z_A f_u^p(x_1, Q^2) + N_A f_u^n(x_1, Q^2) \} B f_{\bar{s}}^p(x_2, Q^2) + [u \leftrightarrow \bar{s}]) \} \} \end{aligned} \quad (7)$$

$$\begin{aligned} S^i(A, x_1) S^j(B, x_2) f_i^N(x_1, Q^2) f_j^N(x_2, Q^2) \frac{d\hat{\sigma}_{ij}^{W^-}}{dy} = & K \frac{2\pi}{3} \frac{G_F}{\sqrt{2}} \frac{x_1 x_2}{AB} \{ \\ & \times \cos^2 \theta_C (S^{\bar{u}}(A, x_1) S^d(B, x_2) \{ Z_A f_{\bar{u}}^p(x_1, Q^2) + N_A f_{\bar{u}}^n(x_1, Q^2) \} \\ & \times \{ Z_B f_d^p(x_2, Q^2) + N_B f_d^n(x_2, Q^2) \} + [\bar{u} \leftrightarrow d]) \\ & + \sin^2 \theta_C (S^{\bar{u}}(A, x_1) S^s(B, x_2) \{ Z_A f_{\bar{u}}^p(x_1, Q^2) + N_A f_{\bar{u}}^n(x_1, Q^2) \} B f_s^p(x_2, Q^2) + [\bar{u} \leftrightarrow s]) \} \} \end{aligned} \quad (8)$$

for each vector boson where  $Z_A$  and  $N_A$  are the proton and neutron numbers in nucleus  $A$  and we have abbreviated the shadowing functions as  $S^i(A, x)$ . We have included a theoretical  $K$  factor,  $K \simeq 1 + 8\pi\alpha_s(Q^2)/9$ , to account for the size of the next-to-leading order corrections<sup>1</sup>. At  $Q = m_V$ ,  $K \sim 1.35$  when  $\alpha_s$  is evaluated at one loop with five active flavors. We note that the  $K$  factor is actually not just a trivial multiplicative factor because in addition to virtual corrections to  $q\bar{q}' \rightarrow V$ , we also have processes with an accompanying jet in the

---

<sup>1</sup>The next-to-next-to-leading order  $W^\pm$  and  $Z^0$  total cross sections have been calculated [18]. These  $\mathcal{O}(\alpha_s^2)$  effects are on the few percent level even though the vector boson can now be produced in the  $gg$  channel.

final state, *e.g.*  $q\bar{q}' \rightarrow Vg$  and  $qg \rightarrow Vq'$ . These real corrections not only smear the  $x_1$  and  $x_2$  values but also introduce the nuclear gluon distribution in the latter process. However, we have shown that the differences between the Drell-Yan, where  $V$  is a virtual photon, shadowing ratios at leading and next-to-leading order are trivial [2]. At the higher scale of  $Z^0$  and  $W^\pm$  production, the approximation should be even better.

Since our calculation is at leading order, we use the MRST LO [19] nucleon parton distributions. The MRST LO parton distribution functions evaluated at  $Q = m_Z$  are shown in Fig. 1. The valence distributions are somewhat larger than the corresponding sea quark distributions at  $x \geq 0.1$  and extend to higher  $x$  values while the sea quarks dominate the valence quarks at  $x \sim 10^{-4}$  by a factor of  $\sim 100$ . Note also that  $f_d^p$  is larger than  $f_u^p$  for  $x > 0.01$ .

The shadowing effect is studied with three parameterizations of the average, homogeneous, shadowing,  $S_k^i(A, x, Q^2)$   $k = 1 - 3$ , measured in nuclear deep-inelastic scattering. The first,  $S_1(A, x)$ , assumes that the quark, gluon and antiquark modifications are equal and includes no  $Q^2$  evolution [20]. The second,  $S_2^i(A, x, Q^2)$ , has separate modifications for the valence quarks, sea quarks and gluons and includes  $Q^2$  evolution from  $2 < Q < 10$  GeV [21]. The third parameterization,  $S_3^i(A, x, Q^2)$ , is based on the GRV LO [22] parton densities. The ratios are evolved over  $1.5 < Q < 100$  GeV [23,24] assuming that  $S_3^{uv} = S_3^{dv}$  and  $S_3^u = S_3^d$  while the heavier sea quarks are evolved separately. Both the  $S_2$  and  $S_3$  ratios are evolved to higher  $Q^2$  using DGLAP evolution [21,23,24]. The initial gluon ratio in  $S_3$  shows significant antishadowing for  $0.1 < x < 0.3$  while the sea quark ratios are shadowed. In contrast,  $S_2$  has less gluon antishadowing and essentially no sea quark effect in the same  $x$  region. However, the  $Q^2$  evolution of  $S_2$  stops below the vector boson mass, rendering it less valuable. We show results with all three parameterizations because no nuclear DIS data is available at high  $Q^2$ . However, since  $S_3$  includes the most recent nuclear DIS data and is evolved to a scale compatible with the vector boson masses, it should perhaps be favored.

The shadowing ratios in a lead nucleus compared to a proton are shown in Fig. 2. The effects of shadowing on the valence quarks is strongest with  $S_1$  since all quarks are treated equivalently. The  $S_2$  and  $S_3$  valence ratios are rather similar in magnitude although the anti-shadowing range,  $0.01 < x < 0.3$  is broadest for  $S_3$  while the  $S_3$  ratio is lower than the  $S_2$  ratio at low  $x$ . The sea quark ratios are very similar for  $S_1$  and  $S_2$  when  $x < 0.1$ . Then the  $S_2$  ratio is essentially unity until  $x > 0.3$ . It is most interesting to note the difference between the light and strange sea ratios in the  $S_3$  parameterization. The ratios  $S_3^u$  and  $S_3^d$  show no antishadowing effect and instead decrease when  $x > 0.1$  while  $S_3^s$  is typically larger over all  $x$  and is antishadowed when  $0.01 < x < 0.2$ . Since all three  $S_3$  sea ratios are equivalent at  $Q = 1.5$  GeV, the difference is solely due to the DGLAP evolution.

To include the spatial dependence of shadowing, we assume that the inhomogeneous shadowing is proportional to the undisturbed local nuclear rest density, Eq. (3), [16]

$$S_{k\text{WS}}^i = S_k^i(A, x, Q^2, \vec{r}, z) = 1 + N_{\text{WS}}[S_k^i(A, x, Q^2) - 1] \frac{\rho(s)}{\rho_0} \quad (9)$$

where  $N_{\text{WS}}$  is a normalization constant chosen such that  $(1/A) \int d^3s \rho(s) S_{k\text{WS}}^i = S_k^i$ . At large radii,  $s \gg R_A$ , medium modifications weaken and the nucleons behave as if they were free. At the center of the nucleus, the modifications are larger than the average value determined from nuclear DIS. A second spatial parameterization,  $S_{k\rho}^i$ , based on the thickness

of a spherical nucleus at the collision point [2], leads to slightly larger modifications in the nuclear core.

We can now use Eqs. (6)-(8) to calculate the  $Z^0$ ,  $W^+$  and  $W^-$  cross sections in nuclear collisions. Table 1 gives the total cross sections in the CMS and ALICE central acceptances  $|y| < 2.4$  and  $|y| < 1$  respectively. The cross sections are larger than the virtual photon mediated Drell-Yan cross sections at lower masses [2]. The results, given for Pb+Pb collisions, are integrated over impact parameter in units of  $\mu b$ /nucleon pair. We note that with the normalization of  $S_{ws}$ , the impact-parameter integrated cross section is unchanged when the spatial dependence is included.

In Table 2 we show the expected rate in nucleus-nucleus collisions at  $b = 0$ ,  $N(S = S_k) = \sigma_{NN} T_{\text{PbPb}}(0) L_{\text{PbPb}}^{\text{int}} \sigma(S = S_k)$  with  $L_{\text{PbPb}}^{\text{int}} = 2.59/\text{nb}$  in a one month LHC run,  $\sigma_{NN} = 60 \text{ mb}$  at LHC energies and  $T_{\text{PbPb}}(0) = 30.4/\text{mb}$ . The absolute numbers in the experimental acceptances are large but do not reflect the measurable decay channels. Including the 3.37% lepton pair branching for  $Z^0$  decays reduces the number produced with no shadowing,  $S = 1$ , to 2450 in CMS and 990 in ALICE. The 10% lepton branching ratio for  $W^+$  and  $W^-$  leaves nearly  $10^4$  observable decays in CMS and 4000 in ALICE.

Figures 3 and 4 compare the ratios of  $Z^0$  and  $W^+$  production in Pb+Pb collisions with the three shadowing parameterizations to Pb+Pb collisions with no shadowing as a function of rapidity. The isospin effects wash out the differences between the  $W^+$  and  $W^-$  distributions in the ratios so that the results are essentially identical for the two charged vector bosons. Therefore the ratios are shown only for the  $W^+$ . The results are shown for several impact parameter bins, the most central bin,  $b < 0.2R_A$ , an intermediate impact parameter bin around  $b \sim R_A$ , and a peripheral bin around  $b \sim 2R_A$ . It is clear that by neglecting the impact parameter dependence of shadowing, one may make an overestimate of the effect in peripheral collisions, an important point if using the  $Z^0$  as a baseline in different transverse energy bins. Note also that the integration over all impact parameters is equivalent to the average shadowing, as expected from the normalization of Eq. (9).

The ratios are rather similar for all vector bosons. The  $S_1$  and  $S_2$  ratios are approximately equal as a function of rapidity, presumably because the  $Q^2$  evolution of the  $S_2$  parameterization ends at  $Q = 10 \text{ GeV}$ . The calculations have been extended over the entire rapidity range of vector boson production. At  $y_Z \sim 0$ ,  $x_1 = x_2 = 0.017$ , in the low  $x$  region. As rapidity increases,  $x_1$  increases, going through the antishadowing region and the EMC region with  $x_1 \sim 0.33$  at  $y_Z = 3$ . When  $y_Z \rightarrow 4$ ,  $x_1 \rightarrow 1$ , entering the “Fermi motion” region and causing the upturn of the ratios at large  $y_Z$ . Note also that at large  $x_1$ , the valence quarks dominate. While increasing  $y_Z$  ( $x_1$ ) traces out the large  $x$  portion of the shadowing curve, the low  $x$  part of the shadowing regime is accessible in  $x_2$  with growing  $y_Z$ . At  $y_Z = 3$ ,  $x_2 \sim 8 \times 10^{-4}$ , in a range where shadowing saturates in  $S_1$  and  $S_2$ . There is no saturation built into the  $S_3$  parameterization, causing a steeper decrease in the ratios for large  $y_Z$  with this parameterization than with  $S_1$  and  $S_2$ . In addition, the  $S_3$  sea quark shadowing is never as strong at low  $x$  as for  $S_1$  and  $S_2$  so that these two parameterizations are both more shadowed in total. The  $Z^0$  ratios are all slightly higher than those for  $W^\pm$  because the larger mass of the  $Z^0$  results in  $x_Z \sim 1.1x_W$ .

The shadowing ratios are fairly simply traced out for vector boson production, especially at leading order since the fixed boson mass defines  $x$  at any  $y$  whereas Drell-Yan shadowing effects are smeared over the mass interval. However, the ratios shown in Figs. 3 and 4 will

not be accessible experimentally due to the nuclear isospin. The comparison must be made to  $pp$  interactions, preferably at the same energy to retain the same  $x$  values. This ideal situation may not be realized for some time at the LHC. Therefore in Figs. 5-7 we show the  $Pb+Pb$  rapidity distributions with and without homogeneous shadowing as well as the distributions from  $pp$  collisions at 14 TeV for all three vector bosons. Note that the  $Pb+Pb$  cross sections are given per nucleon pair for a more direct comparison. The first obvious thing to note is that the higher energy extends the available vector boson rapidity space by one unit. The three gauge bosons all show a similar trend—a rise over the first several units of rapidity, followed by a decrease as the edge of phase space is approached. This type of rapidity distribution is typical for  $q\bar{q}$  dominated processes and is due to the increasing importance of valence quarks at large  $y$  ( $x_1$ ). The strongest effect is for  $W^+$  production, particularly in  $pp$  collisions, and  $W^-$  production in  $Pb+Pb$  collisions because the  $u$  valence quarks carry more momentum than the  $d$  valence, see Fig. 1 (a), causing a strong increase in  $W^+$  production in  $pp$  collisions. The trend appears in  $W^-$  production due to the neutron excess in  $Pb+Pb$  where, in  $nn$  collisions,  $W^-$  production proceeds dominantly through  $f_u^n f_d^n \rightarrow f_d^p f_u^p$ . Likewise, the strength of the rise in  $W^+$  production in  $Pb+Pb$  relative to  $pp$  collisions is somewhat reduced by the neutron content of the nucleus.

Finally, the ratios of the  $Pb+Pb$ /nucleon pair to  $pp$  cross sections are shown in Figs. 8-10 for homogeneous shadowing. Due to the higher  $pp$  cross sections, the ratios are lower than those to  $S = 1$  at 5.5 TeV shown in Figs. 3 and 4. However, one should still be able to distinguish between the shadowing parameterizations and get a handle on the quark shadowing at  $Q = m_V$ , particularly since the 14 TeV  $pp$  data should be available with high statistics. Note that comparing the  $pp$  results to the  $Pb+Pb$  calculations with inhomogeneous shadowing would produce results similar to those shown in Figs. 3 and 4 for different impact parameter bins.

Once the basic nuclear shadowing effects on vector boson production have been understood, they can perhaps be used to study other medium effects in heavy ion collisions by comparing the leptonic and hadronic decay channels. The hadronic decays of the vector bosons,  $\sim 70\%$  of all decays of each boson, may be more difficult to interpret. While the width of the  $Z^0$  decay to  $l^+l^-$  is not expected to be modified in the quark-gluon plasma [25], the  $Z^0$  has a 2.49 GeV total width and will decay in any quark-gluon plasma to two jets through  $Z^0 \rightarrow q\bar{q} \rightarrow \text{jet} + \text{jet}$  in  $\sim 0.1$  fm. Therefore, the decay jets could be modified in the medium which may still be progressing toward thermalization and will be subject to rescattering and jet quenching. Thus a comparison of a reconstructed  $Z^0$  in the dilepton channel where no nuclear effects are expected since leptons do not interact strongly and medium-modified jets should result in a broader width for the  $q\bar{q}$  channel than the  $l^+l^-$  channel [26]. In addition, the  $Z^0$  could be used to tag jets through the  $q\bar{q} \rightarrow Z^0g$  and  $gq \rightarrow Z^0q$  channels to study the jet properties in the quark-gluon plasma [7].

**Acknowledgements** I thank K.J. Eskola for providing the shadowing parameterizations. I thank D. Kharzeev, K. Redlich and U. Wiedemann for discussions.

## REFERENCES

- [1] K.J. Eskola, K. Kajantie and J. Lindfors, Nucl. Phys. **B323**, 37 (1989).
- [2] V. Emel'yanov, A. Khodinov, S.R. Klein and R. Vogt, Phys. Rev. **C56**, 2726 (2000).
- [3] R. Vogt, Phys. Rept. **310**, 197 (1999).
- [4] H. Satz, Rept. Prog. Phys. **63**, 1511 (2000).
- [5] Z. Lin and R. Vogt, Nucl. Phys. **B544**, 339 (1999).
- [6] J. Gunion and R. Vogt, Nucl. Phys. **B492**, 301 (1997).
- [7] V. Kartvelishvili, R. Kvavadze and R. Shanidze, Phys. Lett. **356**, 589 (1995).
- [8] V. Emel'yanov, A. Khodinov, S.R. Klein and R. Vogt, Phys. Rev. Lett. **81**, 1801 (1998).
- [9] F. Abe *et al.*, Phys. Rev. Lett. **81**, 5754 (1998).
- [10] C.W. deJager, H. deVries and C. deVries, Atomic Data and Nuclear Data Tables **14**, 485 (1974).
- [11] J.J. Aubert *et al.*, Nucl. Phys. **B293**, 740 (1987); M. Arneodo, Phys. Rept. **240**, 301 (1994).
- [12] L.V. Gribov, E.M. Levin and M.G. Ryskin, Phys. Rept. **100**, 1 (1983).
- [13] S. Kumano and F.E. Close, Phys. Rev. C **41**, 1855 (1990).
- [14] T. Kitagaki *et al.*, Phys. Lett. **214**, 281 (1988).
- [15] K.J. Eskola, Z. Phys. C **51**, 633 (1991).
- [16] V. Emel'yanov, A. Khodinov, S.R. Klein, and R. Vogt, Phys. Rev. **C56**, 2726 (1997).
- [17] V. Emel'yanov, A. Khodinov, S.R. Klein, and R. Vogt, Phys. Rev. **C59**, 1860 (1999).
- [18] R. Hamberg, W.L. van Neerven and T. Matsuura, Nucl. Phys. **B359**, 343 (1991).
- [19] A.D. Martin, R.G. Roberts, and W.J. Stirling, and R.S. Thorne, Eur. Phys. J. **C4**, 463 (1998); Phys. Lett. **B443**, 301 (1998).
- [20] K.J. Eskola, J. Qiu and J. Czyzewski, private communication.
- [21] K.J. Eskola, Nucl. Phys. **B400**, 240 (1993).
- [22] M. Glück, E. Reya, and A. Vogt, Z. Phys. **C53**, 127 (1992).
- [23] K.J. Eskola, V.J. Kolhinen and P.V. Ruuskanen, Nucl. Phys. **B535**, 351 (1998).
- [24] K.J. Eskola, V.J. Kolhinen and C.A. Salgado, Eur. Phys. J. **C9**, 61 (1999).
- [25] J.I. Kapusta and S.M.H. Wong, Phys. Rev. **D62**, 037301 (2000).
- [26] W. Geist, private communication.

## TABLES

Detector	$\sigma(S = 1)$ (nb)	$\sigma(S = S_1)$ (nb)	$\sigma(S = S_2)$ (nb)	$\sigma(S = S_3)$ (nb)
$Z^0$				
CMS	15.41	10.87	10.96	14.26
ALICE	6.22	4.35	4.49	5.86
$W^+$				
CMS	20.85	14.39	14.54	18.93
ALICE	8.13	5.52	5.73	7.44
$W^-$				
CMS	21.84	15.08	15.26	19.83
ALICE	8.35	5.66	5.89	7.64

TABLE I. Vector boson production cross sections in units of nb per nucleon pair in Pb+Pb collisions at 5.5 TeV/nucleon calculated with the MRST LO parton densities. Full azimuthal coverage is assumed. The corresponding  $pp$  cross sections at 14 TeV are  $\sigma^{Z^0} = 32.8$  nb (CMS), 13.34 nb (ALICE),  $\sigma^{W^+} = 45.6$  nb (CMS), 17.46 nb (ALICE) and  $\sigma^{W^-} = 38.46$  nb (CMS), 15.68 nb (ALICE).

Detector	$N(S = 1)$	$N(S = S_1)$	$N(S = S_2)$	$N(S = S_3)$
$Z^0$				
CMS	$7.28 \times 10^4$	$5.14 \times 10^4$	$5.18 \times 10^4$	$6.74 \times 10^4$
ALICE	$2.94 \times 10^4$	$2.06 \times 10^4$	$2.12 \times 10^4$	$2.76 \times 10^4$
$W^+$				
CMS	$9.85 \times 10^4$	$6.80 \times 10^4$	$6.87 \times 10^4$	$8.94 \times 10^4$
ALICE	$3.84 \times 10^4$	$2.61 \times 10^4$	$2.71 \times 10^4$	$3.51 \times 10^4$
$W^-$				
CMS	$1.03 \times 10^5$	$7.12 \times 10^4$	$7.21 \times 10^4$	$9.37 \times 10^4$
ALICE	$3.94 \times 10^4$	$2.67 \times 10^4$	$2.78 \times 10^4$	$3.61 \times 10^4$

TABLE II. Number of vector bosons produced at  $b = 0$  in a one month ( $10^6$  s) Pb+Pb LHC run at 5.5 TeV/nucleon.

FIGURES

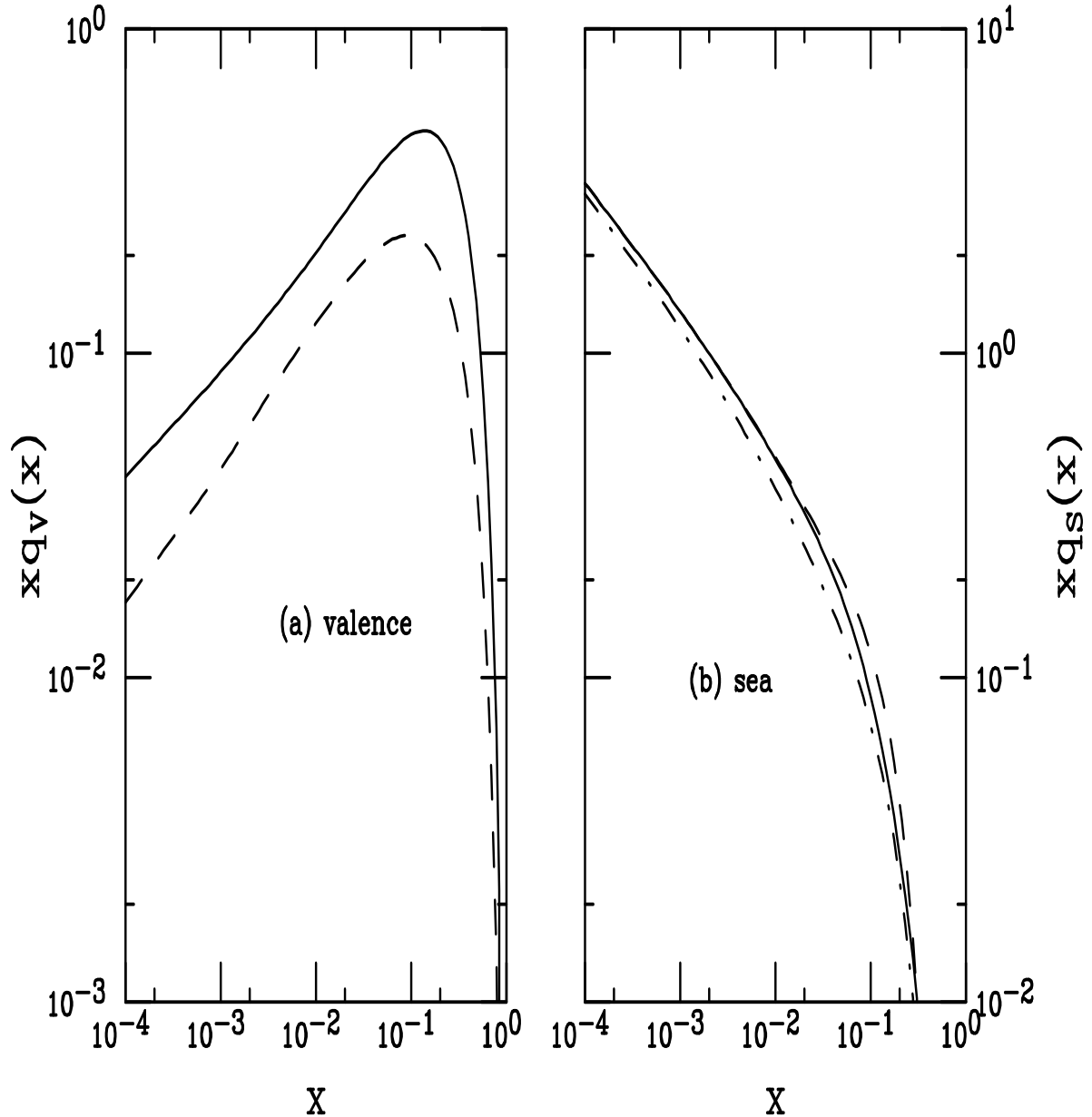


FIG. 1. The MRST LO proton parton distribution functions evaluated at  $Q = m_Z$ . The up (solid) and down (dashed) valence distributions are given in (a) while the up (solid), down (dashed), and strange (dot-dashed) sea quark distributions are shown in (b).

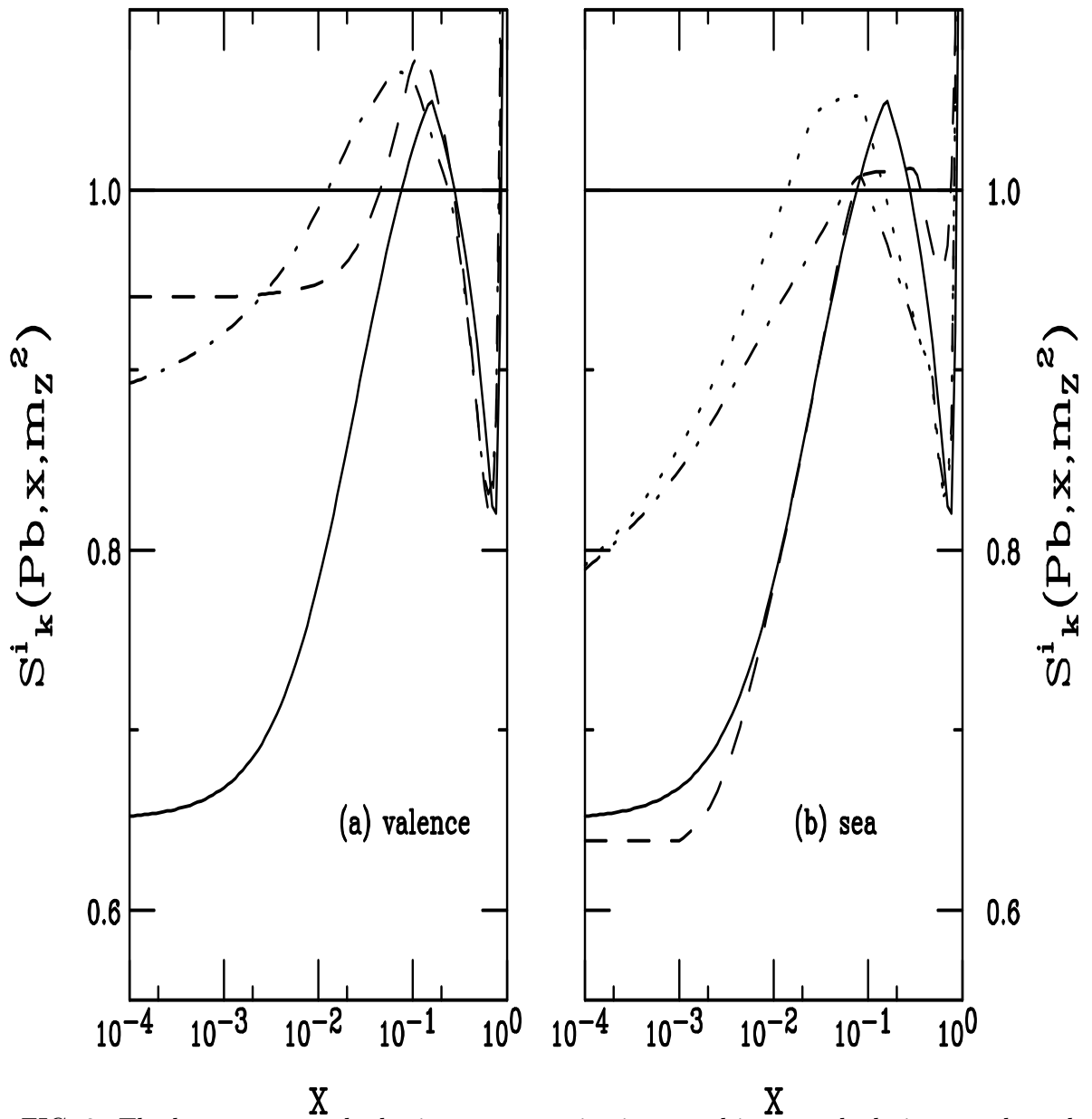


FIG. 2. The homogeneous shadowing parameterizations used in our calculations, evaluated at  $Q = m_Z$ . Valence shadowing is shown in (a) for the  $S_1$  (solid),  $S_2$  (dashed), and  $S_3$  (dot-dashed) parameterizations. Sea quark shadowing is shown in (b) for  $S_1$  (solid),  $S_2$  (dashed),  $S_3^u = S_3^d$  (dot-dashed) and  $S_3^s$  (dotted).

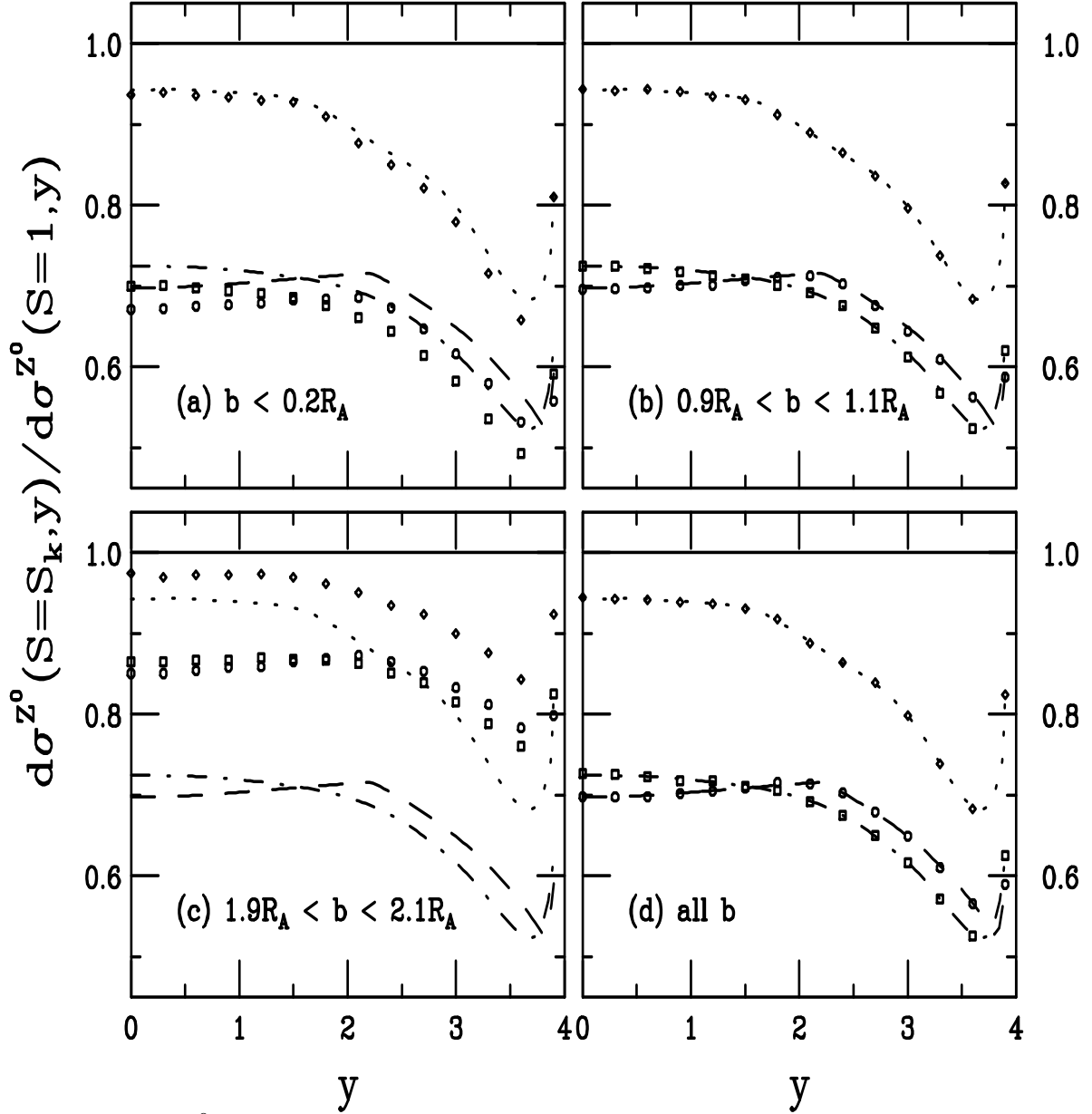


FIG. 3. The  $Z^0$  rapidity distributions, relative to  $S = 1$  for Pb+Pb collisions at the LHC, calculated with the MRST LO distributions. Central,  $b < 0.2R_A$ , semi-central,  $0.9R_A < b < 1.1R_A$ , peripheral,  $1.9R_A < b < 2.1R_A$  impact parameters are shown along with the integral over all  $b$ . The homogeneous shadowing results are given in the dashed,  $S_1$ , dot-dashed,  $S_2$ , and dotted,  $S_3$ , lines. The inhomogeneous shadowing ratios for  $S_{1\text{ WS}}$ , circles,  $S_{2\text{ WS}}$ , squares, and  $S_{3\text{ WS}}$ , diamonds, are also shown.

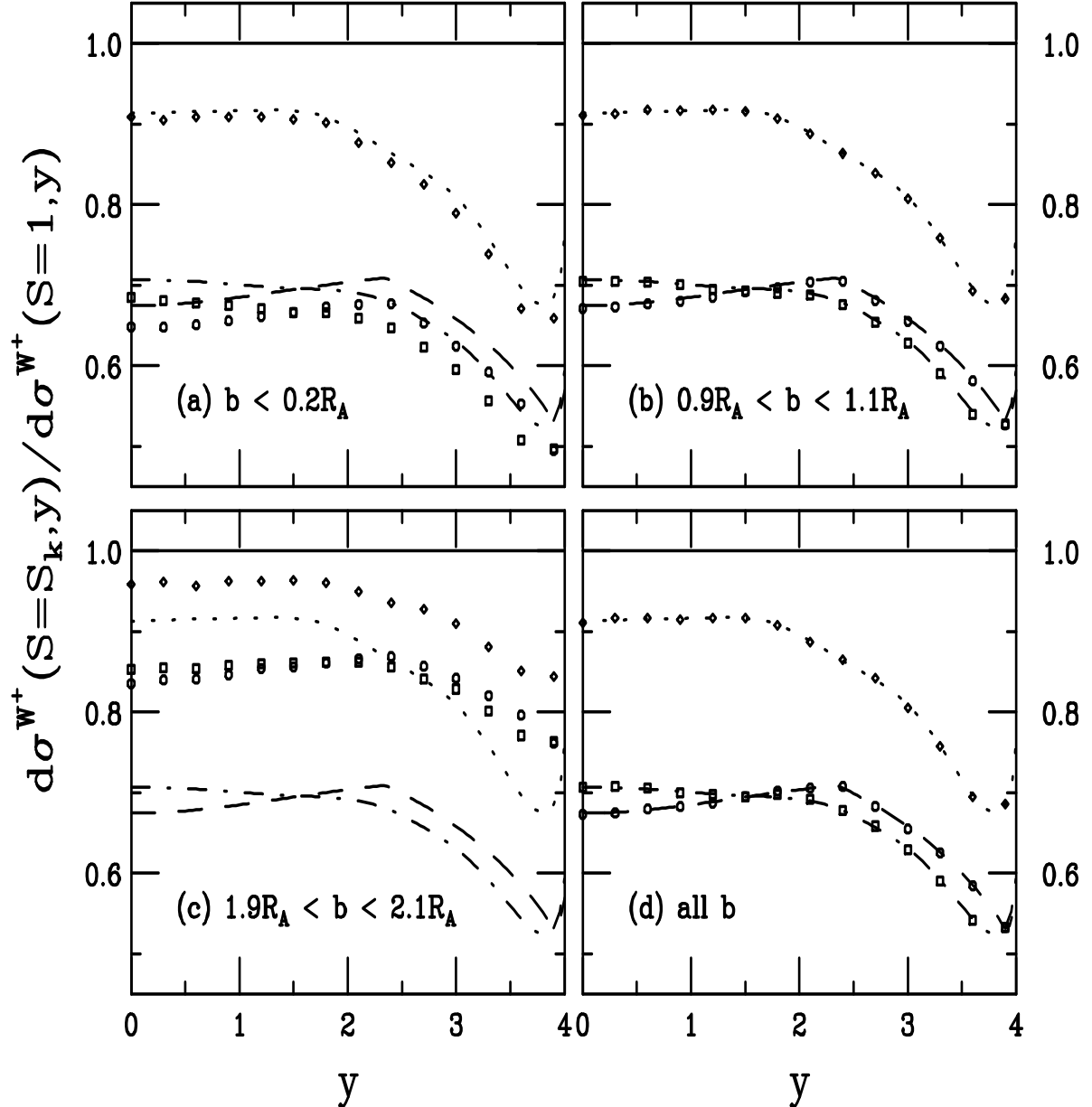


FIG. 4. The  $W^+$  rapidity distributions, relative to  $S = 1$  for Pb+Pb collisions at the LHC, calculated with the MRST LO distributions. Central,  $b < 0.2R_A$ , semi-central,  $0.9R_A < b < 1.1R_A$ , peripheral,  $1.9R_A < b < 2.1R_A$  impact parameters are shown along with the integral over all  $b$ . The homogeneous shadowing results are given in the dashed,  $S_1$ , dot-dashed,  $S_2$ , and dotted,  $S_3$ , lines. The inhomogeneous shadowing ratios for  $S_1$  WS, circles,  $S_2$  WS, squares, and  $S_3$  WS, diamonds, are also shown.

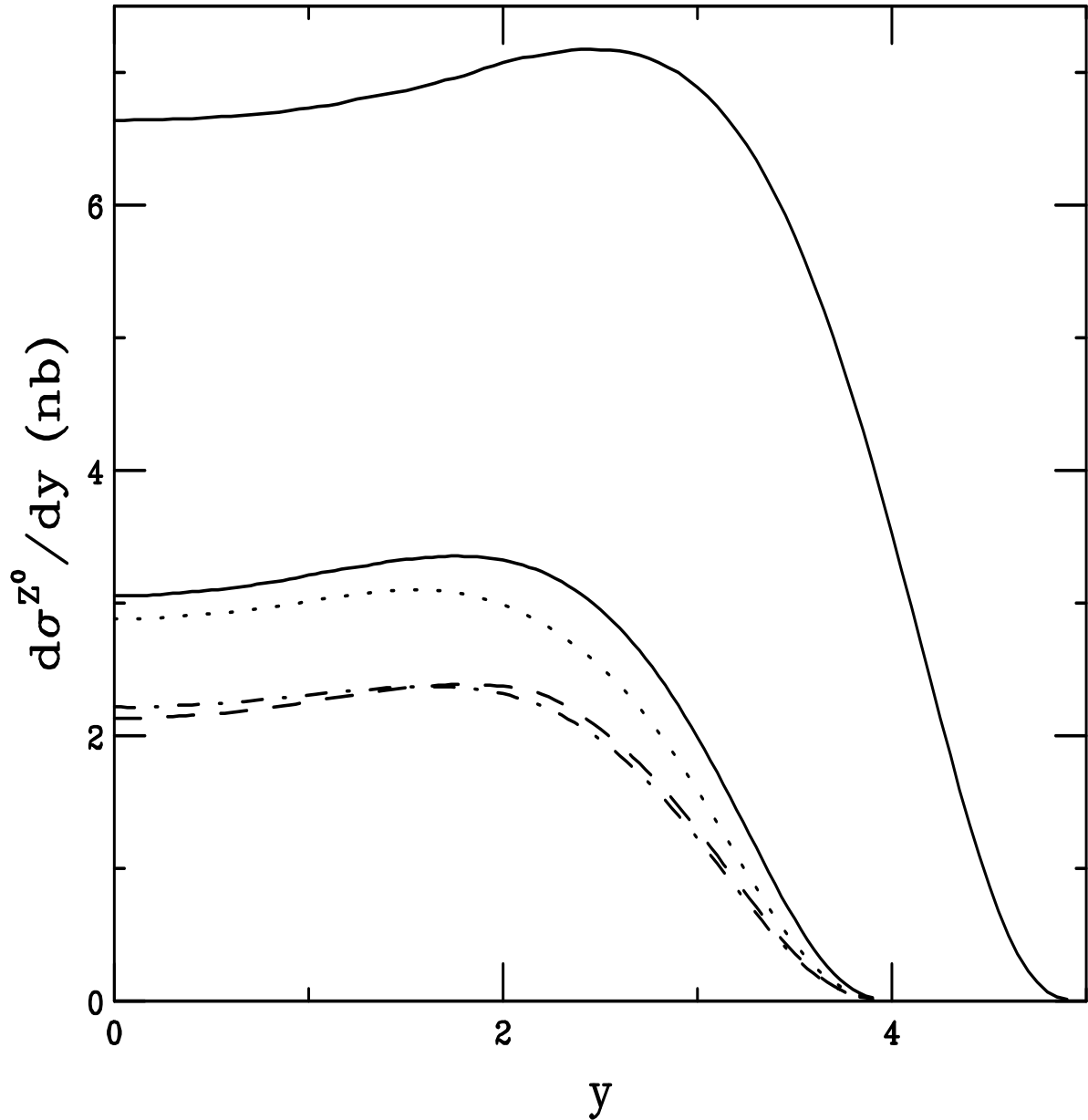


FIG. 5. The  $Z^0$  rapidity distributions in  $pp$  and  $Pb+Pb$  collisions, calculated with the MRST LO distributions. The upper solid curve is the  $pp$  result at 14 TeV while the lower solid curve is the  $Pb+Pb$  distribution at 5.5 TeV/nucleon pair with no shadowing. The homogeneous shadowing results for  $Pb+Pb$  collisions are given in the dashed,  $S_1$ , dot-dashed,  $S_2$ , and dotted,  $S_3$ , lines.

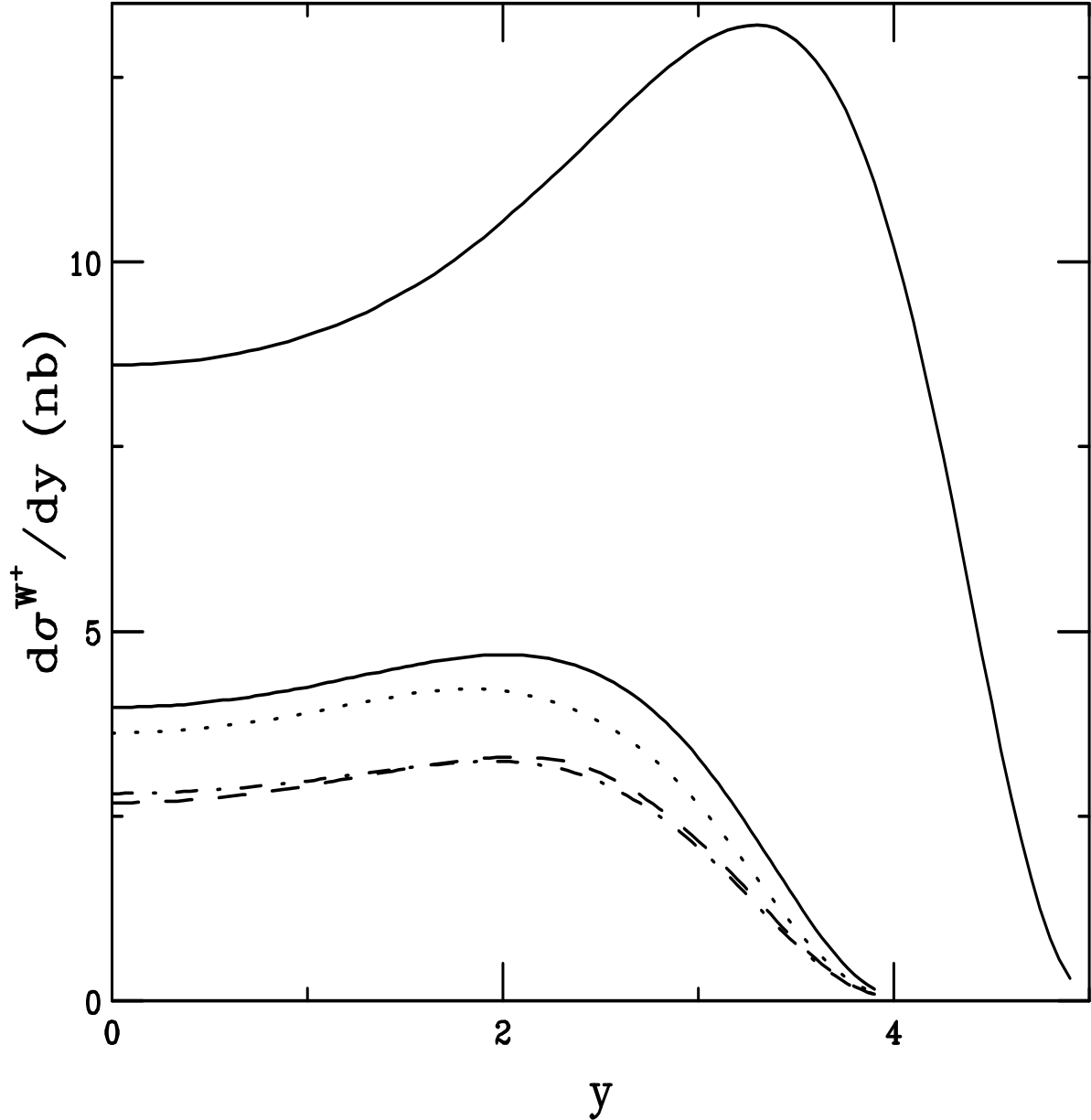


FIG. 6. The  $W^+$  rapidity distributions in  $pp$  and  $Pb+Pb$  collisions, calculated with the MRST LO distributions. The upper solid curve is the  $pp$  result at 14 TeV while the lower solid curve is the  $Pb+Pb$  distribution at 5.5 TeV/nucleon pair with no shadowing. The homogeneous shadowing results for  $Pb+Pb$  collisions are given in the dashed,  $S_1$ , dot-dashed,  $S_2$ , and dotted,  $S_3$ , lines.

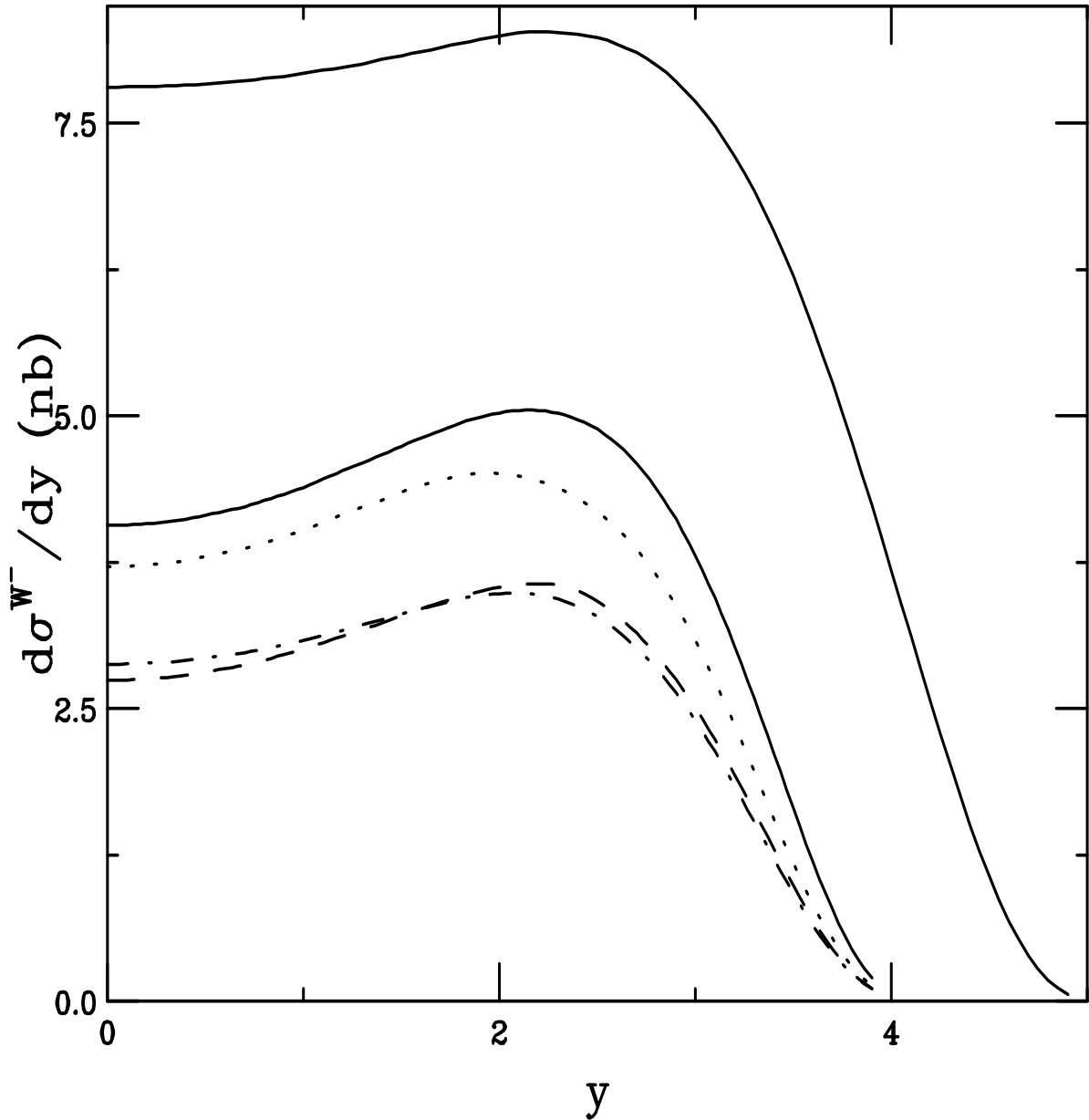


FIG. 7. The  $W^-$  rapidity distributions in  $pp$  and  $Pb+Pb$  collisions, calculated with the MRST LO distributions. The upper solid curve is the  $pp$  result at 14 TeV while the lower solid curve is the  $Pb+Pb$  distribution at 5.5 TeV/nucleon pair with no shadowing. The homogeneous shadowing results for  $Pb+Pb$  collisions are given in the dashed,  $S_1$ , dot-dashed,  $S_2$ , and dotted,  $S_3$ , lines.

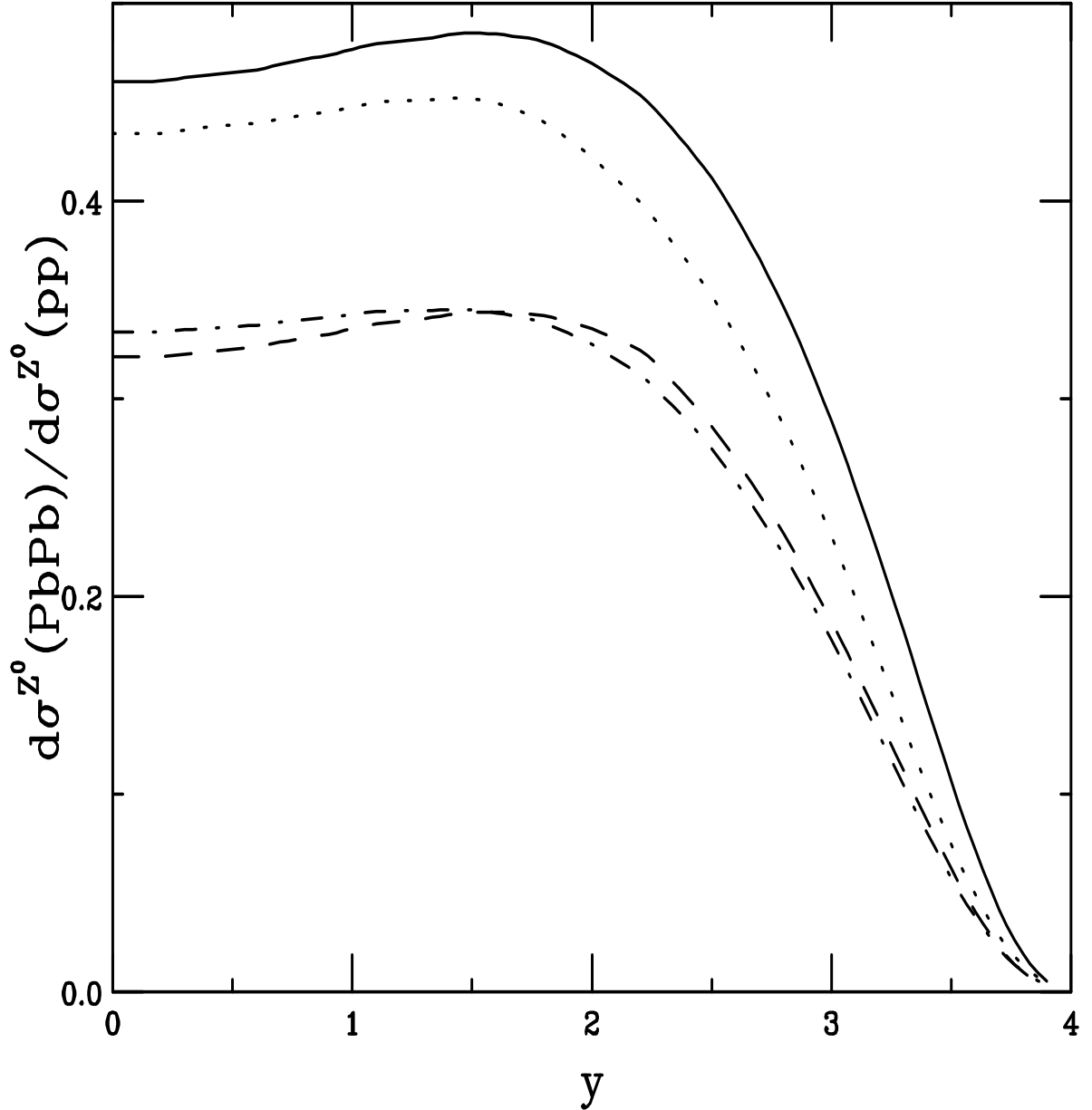


FIG. 8. The ratios of the  $Z^0$  rapidity distributions in Pb+Pb collisions relative to  $pp$  collisions, calculated with the MRST LO distributions. The solid curve is the ratio without shadowing. The homogeneous shadowing results are given in the dashed,  $S_1$ , dot-dashed,  $S_2$ , and dotted,  $S_3$ , lines.

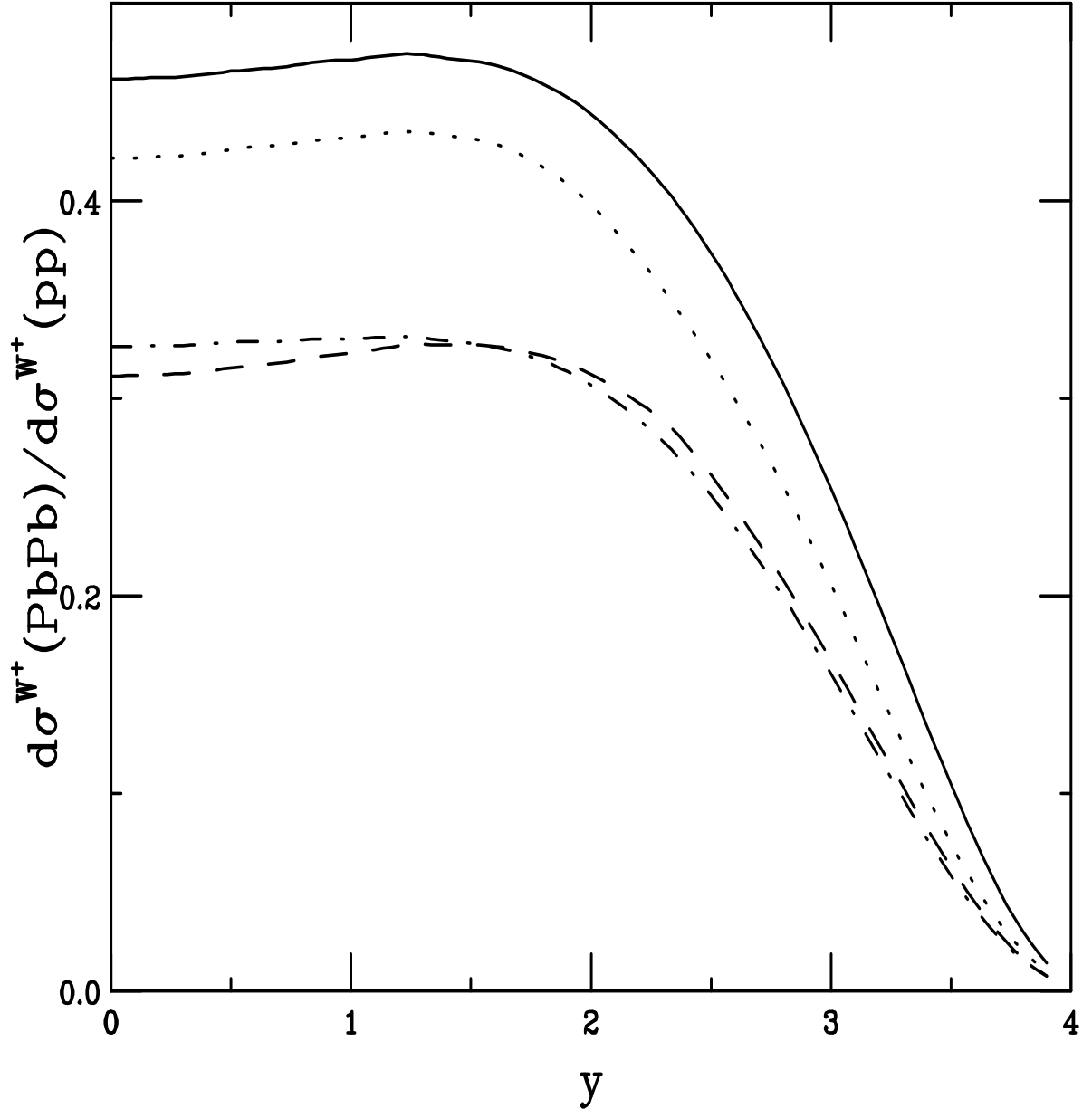


FIG. 9. The ratios of the  $W^+$  rapidity distributions in Pb+Pb collisions relative to  $pp$  collisions, calculated with the MRST LO distributions. The solid curve is the ratio without shadowing. The homogeneous shadowing results are given in the dashed,  $S_1$ , dot-dashed,  $S_2$ , and dotted,  $S_3$ , lines.

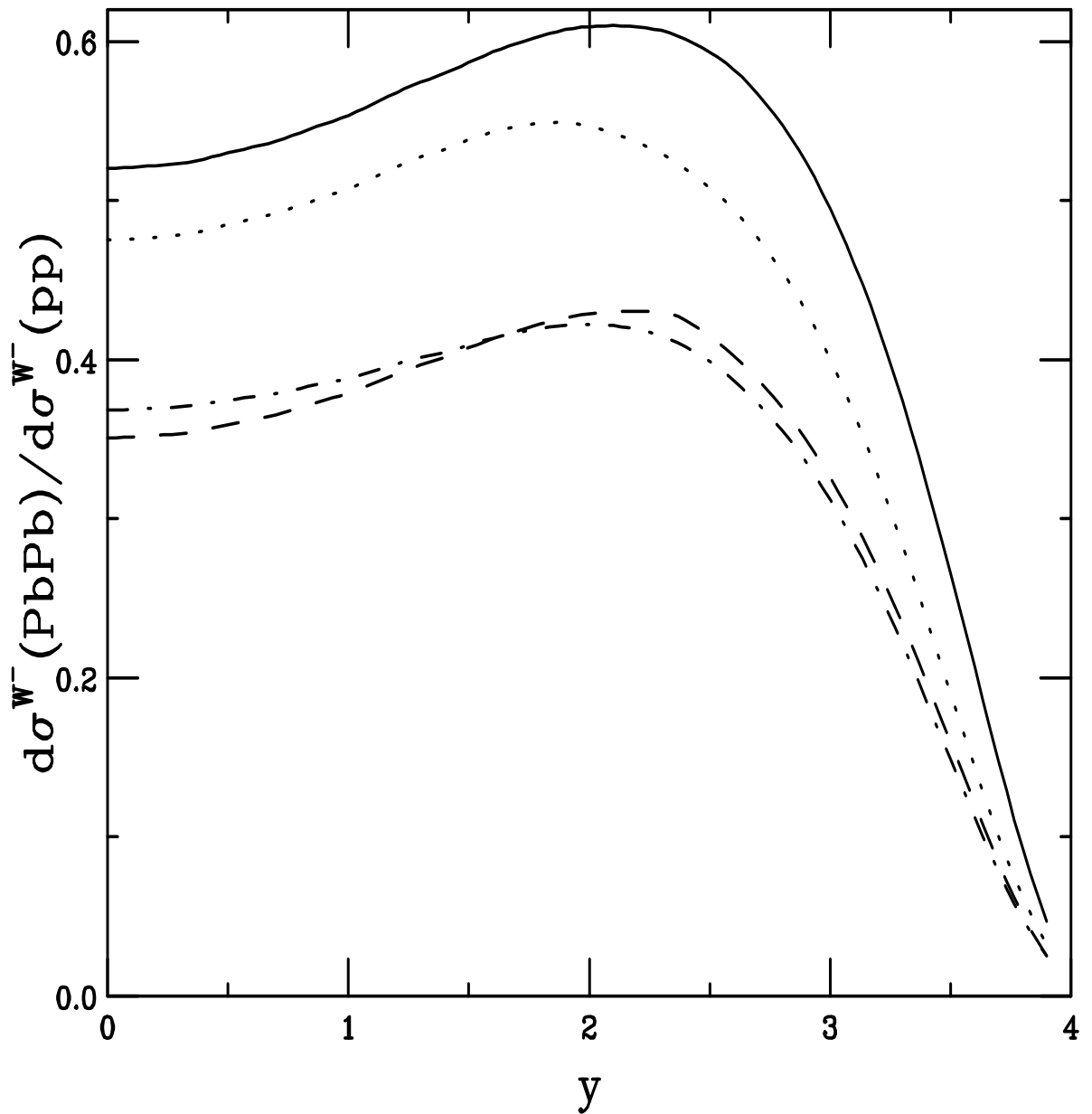


FIG. 10. The ratios of the  $W^-$  rapidity distributions in Pb+Pb collisions relative to  $pp$  collisions, calculated with the MRST LO distributions. The solid curve is the ratio without shadowing. The homogeneous shadowing results are given in the dashed,  $S_1$ , dot-dashed,  $S_2$ , and dotted,  $S_3$ , lines.